Progress In Electromagnetics Research B, Vol. 38, 1–22, 2012

COMPUTATIONALLY EFFICIENT MODEL FOR UWB SIGNAL ATTENUATION DUE TO PROPAGATION IN TISSUE FOR BIOMEDICAL IMPLANTS

P. T. Theilmann[1, *], M. A. Tassoudji[2], E. H. Teague[2], D. F. Kimball[1], and P. M. Asbeck[1]

[1]Department of Electrical and Computer Engineering, University of California at San Diego, La Jolla, CA 92093, USA

[2]Qualcomm Inc., San Diego, CA 92121, USA

Abstract—An analytical model which predicts the attenuation of ultrawide-band (UWB) signals as they traverse various inhomogeneous tissues is presented. The model provides a computationally efficient method of determining the frequency-dependent losses encountered by electromagnetic radio frequency (RF) signals used to communicate with biomedical implants. Classic transmission line theory is employed to generate an analytical representation which models the inhomogeneous tissue using layers of homogeneous material. The proposed model was verified experimentally with tests of both single and multilayer samples. A realistic abdominal implant scenario was also modeled and the predictions were verified using a commercially available 3D electromagnetic (EM) simulator. The results of this study indicate that for deep implants the higher frequency portion of the UWB spectrum is attenuated much more strongly than the lower end of the band. This implies that for robust communication UWB signals targeting biomedical implants should be limited to the lower portion of the spectrum.

1. INTRODUCTION

As wireless medical implants increase in complexity providing improved functionality, higher data rate communication will be required. To this end, IEEE has established the 802.15.6 working group for body area networks (BAN). They are tasked to develop a standard for wireless devices which will be used around, on, and inside

Received 21 November 2011, Accepted 4 January 2012, Scheduled 8 January 2012

* Corresponding author: Paul T. Theilmann (ptheilma@ucsd.edu).

the human body [1]. Ultrawide-band (UWB) signals (3.1–10.6 GHz), which are already standardized as IEEE 802.15.4a for wireless personal area networks (WPAN), provide the possibility of data rates as high as 26 Mbps over short distances [2]. High definition video and hundreds of channels of bio-data streams are just a few of the possibilities available if such a data link could be established. For this reason the UWB band may be used for both the wearable BAN link and the implant BAN link [3].

When designing a wireless implant communication link it is important to model the transmission channel to aid in link margin calculations and overall transceiver design. Many papers have been published on models of antenna structures for implants in the UWB band, but these papers have focused on antenna matching not investigations of channel loss [4–6]. Likewise similar models have been created for lower frequency ISM bands [7].

To date many transmission models in the BAN UWB band have focused on wearable devices [8–10] as well as beamformers [11] and imagers [12], with only a few models targeting implant channels [3, 13, 14]. These papers apply relatively complicated frequency-dependent finite difference time domain (FDTD) techniques. This full wave analysis technique is computationally expensive and makes implant design time consuming and difficult. An analytical model of the transmission channel which can be easily implemented would be important to designers. In [15] and [16] simplified analytical multilayer models which contained some treatment of losses in the signal path, were presented. Both papers presented models focused on UWB radar not implants. Unfortunately, the attenuation calculations in [15] did not take into account reflections between layers and while the work in [16] presented a few key components of an attenuation model, some of the important implementation aspects were not shown.

In this study, a non-uniform transmission line analytical model is adapted for wave propagation and implemented in Matlab. The model calculates the attenuation a signal will encounter as it traverses multilayer biological samples. By modeling the transmission path as individual layers of homogeneous material and combining the results, a simple model for inhomogeneous tissue is created.

This paper is organized as follows. Section 2 gives a derivation of the transmission line analytical model as it applies to traveling waves. In Section 3, the model is verified experimentally using single and multilayer samples of water, beef and a sucrose solution. Section 4 presents a comparison between the proposed transmission line based analytical model and CST Microwave Studio, a commercial 3D finite integration technique (FIT) solver. Both tools are used to investigate a

realistic abdominal implant scenario and the results are compared. The implications of the results on the use of UWB signals for abdominal implants is also discussed. Section 5 contains conclusions.

2. TRANSMISSION LINE BASED ANALYTICAL MODEL

2.1. Transmission Line Theory

It is often important to calculate the signal transmission between source and load for structures such as the one in Figure 1(a) which comprises many transmission lines with varying impedances. Calculating the reflection and transmission at each discontinuity

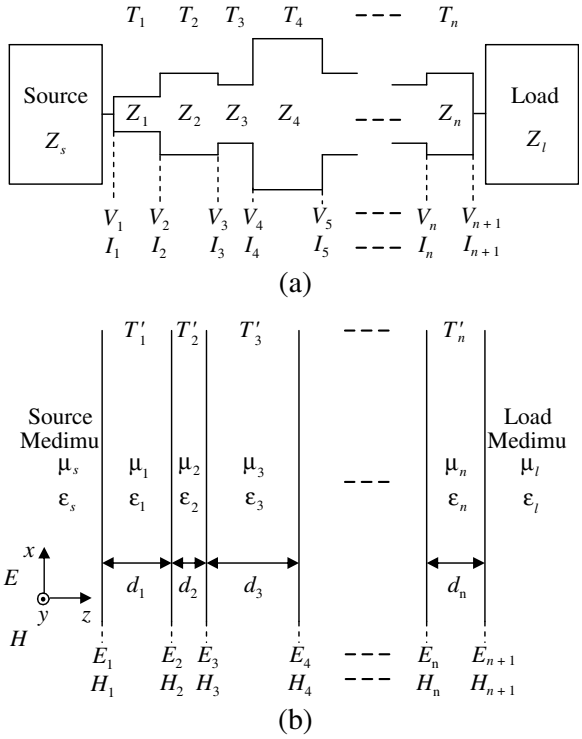

Figure 1. (a) A transmission line of varying impedance. Segments of constant impedance can be modeled using transmission matrices which can be cascaded to represent the entire transmission line. (b) Wave propagation through a non-uniform medium. Modeling techniques analogous to those used for transmission lines can be applied.

quickly becomes tedious as each reflected or transmitted wave encounters the previous or next discontinuity and creates another transmission or reflection. Instead it is more straightforward to calculate the total voltage and current at each discontinuity in terms of the voltage and current at the next discontinuity. Assuming positive current is taken as directed from the source to the load,

$$\begin{bmatrix} V_i \\ I_i \end{bmatrix} = [T_i] \begin{bmatrix} V_{i+1} \\ I_{i+1} \end{bmatrix} \tag{1}$$

where V_i and I_i are the voltage and current at the ith discontinuity. T_i is the transmission matrix sometimes referred to as the $ABCD$ matrix of the ith non-uniform transmission line segment [17].

At boundaries between different transmission lines, the total voltage and current on either side of the discontinuity must be equal. This makes $ABCD$ matrices convenient for transmission lines with several discontinuities because the matrices of each uniform segment can be cascaded to represent the entire non-uniform line.

$$[T_{\text{Total}}] = [T_1][T_2][T_3]\dots[T_n] \tag{2}$$

$$\begin{bmatrix} V_1 \\ I_1 \end{bmatrix} = [T_{\text{Total}}] \begin{bmatrix} V_{n+1} \\ I_{n+1} \end{bmatrix} \tag{3}$$

The matrix $[T_{\text{Total}}]$ in (2) completely defines the non-uniform transmission line of Figure 1(a) as seen by the source and load.

2.2. Application to Wave Propagation

The solutions of classical transmission-line theory can be directly applied to wave propagation problems by making the following analogies [18],

$$V \rightarrow E_x \quad \text{and} \quad I \rightarrow H_y \tag{4}$$

where E_x and H_y are respectively the transverse electric and magnetic field components of the traveling wave. In (4) the axes have been oriented such that for the incoming wave, the electric field points entirely in the positive x-direction and the magnetic field points entirely in the positive y-direction. Thus the wave propagates in the positive z-direction. For this study we will assume that the wave is of normal incidence to the sample surface. Since there will be no rotation of the field as it traverses the medium, the subscripts x and y will be dropped. Therefore with reference to Figure 1(b),

$$\begin{bmatrix} E_1 \\ H_1 \end{bmatrix} = \left[T'_{\text{Total}}\right] \begin{bmatrix} E_{n+1} \\ H_{n+1} \end{bmatrix} \tag{5}$$

where $[T'_{\text{Total}}]$ is the result of the cascade multiplication of the transmission matrices representing each homogeneous section of propagation medium in Figure 1(b).

The total electric field at the ith $+ 1$ discontinuity of Figure 1(b) can be separated into a forward $(+)$ and backward $(-)$ moving wave.

$$E_{i+1} = E_+ + E_- \tag{6}$$

Both E_+ and E_- point in the positive x-direction. Similarly the magnetic field can be written as

$$H_{i+1} = H_+ - H_- = \frac{E_+}{\eta_i} - \frac{E_-}{\eta_i} \tag{7}$$

It should be noted that magnetic component of the forward moving wave (H_+) points in the positive y-direction while the magnetic component of the backward moving wave (H_-) points in the negative y-direction. In (7) η_i is the complex impedance of the ith medium.

$$\eta_i = \sqrt{\frac{\mu_i}{\varepsilon_i}} \tag{8}$$

In (8) μ_i and ε_i are respectively the complex permeability and permittivity of the ith medium. The electric and magnetic field at the ith discontinuity can be found using (6), (7) and telegraphers equations [18],

$$E_i = E_+ e^{\gamma_i d_i} + E_- e^{-\gamma_i d_i} \tag{9}$$

$$H_i = \frac{1}{\eta_i}\left(E_+ e^{\gamma_i d_i} - E_- e^{-\gamma_i d_i}\right) \tag{10}$$

where d_i is the thickness of the ith medium and γ_i is its complex propagation constant.

$$\gamma_i = j\omega\sqrt{\mu_i \varepsilon_i} \tag{11}$$

Here ω refers to the angular frequency of the incoming wave. Using (6), (7), (9) and (10) E_i and H_i can be solved for in terms of E_{i+1} and H_{i+1}.

$$E_i = E_{i+1}\cosh\gamma_i d_i + \eta_i H_{i+1}\sinh\gamma_i d_i \tag{12}$$

$$H_i = \frac{1}{\eta_i} E_{i+1}\sinh\gamma_i d_i + H_{i+1}\cosh\gamma_i d_i \tag{13}$$

The transmission matrix for the ith segment of Figure 1(b) can now be written directly from (12) and (13).

$$\left[T'_i\right] = \begin{bmatrix} A'_i & B'_i \\ C'_i & D'_i \end{bmatrix} = \begin{bmatrix} \cosh\gamma_i d_i & \eta_i \sinh\gamma_i d_i \\ \frac{1}{\eta_i}\sinh\gamma_i d_i & \cosh\gamma_i d_i \end{bmatrix} \tag{14}$$

It is now quite straight forward to calculate the transmission matrix for each homogeneous medium segment of a multilayer transmission

problem such as the one in Figure 1(b). The matrices can then be cascaded using (2) to calculate $[T'_{\text{Total}}]$, the transmission matrix representing the entire inhomogeneous medium.

For this study the quantity of interest is time-average power. The time-average power for a linearly polarized plane wave can be calculated from the Poynting vector [19]

$$P_{av} = \frac{1}{2}\text{Re}\left(EH^*\right). \tag{15}$$

Converting the transmission matrix of (14) to a scattering parameter (S) matrix allows for the direct computation of relevant time-average power ratios.

Most text books assume the source and load impedance are real and equal when computing conversions between transmission and S-parameters [19]. In [20] and [21] arbitrary impedance is accounted for but the incoming and outgoing waves are not normalized to their respective port impedance, leading to results which are not easily converted to time-average power ratios. In [22], complex load and source impedance are assumed, but as pointed out in [23] an unconventional definition of waves is used which results in S-parameters that are inconsistent with those one would measure on a vector network analyzer. Wave definitions which allow for complex source and load impedances are rigorously defined in [24], but conversions between transmission and scattering matrices as defined in this paper are not given. Thus to avoid confusion, the derivation of (16)–(18) using definitions suitable for this work is included in the Appendix.

Total power attenuation caused by the sample is A_{sl} given by

$$\begin{aligned} A_{sl} &= \frac{P_{l+}}{P_{s+}} = A_{ls} = \frac{P_{s-}}{P_{l-}} \\ &= \left| \frac{2\sqrt{\text{Re}(\eta_s)}\sqrt{\text{Re}(\eta_l)}}{\eta_l A'_{\text{Total}} + B'_{\text{Total}} + \eta_s\eta_l C'_{\text{Total}} + \eta_s D'_{\text{Total}}} \right|^2 . \end{aligned} \tag{16}$$

Power reflection at the source interface is R_s given by

$$R_s = \frac{P_{s-}}{P_{s+}} = \left| \frac{\eta_l A'_{\text{Total}} + B'_{\text{Total}} - \eta_s^*\eta_l C'_{\text{Total}} - \eta_s^* D'_{\text{Total}}}{\eta_l A'_{\text{Total}} + B'_{\text{Total}} + \eta_s\eta_l C'_{\text{Total}} + \eta_s D'_{\text{Total}}} \right|^2 . \tag{17}$$

Power reflection at the load interface is R_l given by

$$R_l = \frac{P_{l+}}{P_{l-}} = \left| \frac{-\eta_l^* A'_{\text{Total}} + B'_{\text{Total}} - \eta_s\eta_l^* C'_{\text{Total}} + \eta_s D'_{\text{Total}}}{\eta_l A'_{\text{Total}} + B'_{\text{Total}} + \eta_s\eta_l C'_{\text{Total}} + \eta_s D'_{\text{Total}}} \right|^2 . \tag{18}$$

In the above equations η_s and η_l are the complex impedance of the source and load media respectively. A'_{Total}, B'_{Total}, C'_{Total}, and

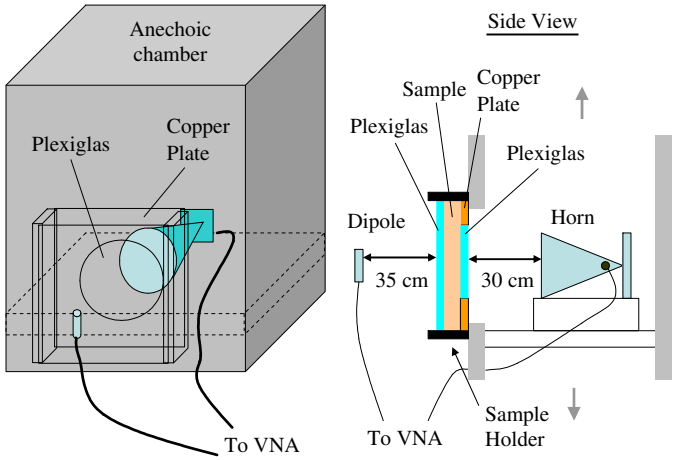

Figure 2. Measurement setup. The receiving horn antenna is placed inside an anechoic chamber and the sample is placed against a window of Plexiglas.

D'_{Total} are the frequency dependent transmission parameters of $[T'_{\text{Total}}]$. Time-average power as defined by (15) is denoted P with subscripts indicating the source (s) or load (l) interface and the positive $z(+)$ or negative $z(-)$ direction.

3. MODEL VERIFICATION

3.1. Experimental Setup

The model was verified experimentally in this work, initially by testing simple structures. The measurement setup is shown in Figure 2. A vector network analyzer (VNA) was used to measure the S-parameters of the dipole (port 1) and horn (port 2) antenna. The measured S_{11} of both antennas with no sample present is shown in Figure 3. The measurement was also performed with various samples present and the effect on S_{11} was negligible at both ports. In this experimental setup the source and load impedance at the antenna ports is real, thus (as explained in the Appendix) $A_{sl} = A_{ls} = |S_{21}|^2$. Attenuation ($A$) due to the sample is defined as the path loss with the sample minus the path loss with the sample removed from the holder, leaving an air gap in its place.

$$\begin{aligned} A &= -\left|S_{21\,\text{sample}}\right|^2 \text{ (dB)} + \left|S_{21\,\text{air}}\right|^2 \text{ (dB)} \\ &= -A_{sl\_\text{sample}} \text{ (dB)} + A_{sl\_\text{air}} \text{ (dB)} \end{aligned} \tag{19}$$

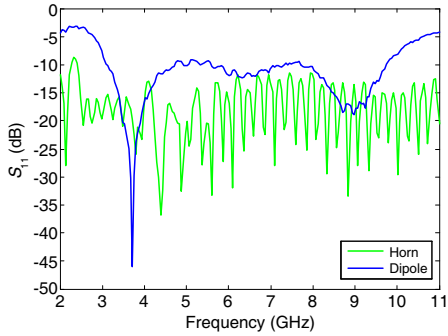

Figure 3. Measured S_{11} of the dipole antenna and horn antenna used in the experiment.

Calculating A in this way removes the effects of antenna inefficiency and path loss in air, leaving only the added attenuation caused by the presence of the sample. Also note that A (dB) is made to be positive.

UWB signals contain high frequencies which easily reflect off nearby objects creating multipaths. For implants all signal paths between the antennas must traverse the tissue in which the implant is enclosed. Thus in the experimental setup great care must be taken to ensure that signal power does not bypass the sample as it is transmitted between ports. To this end the horn antenna is placed within an anechoic chamber while the dipole antenna is placed outside of the chamber, see Figure 2. A square 40×40 cm hole in the side of the chamber is used as a window for signals to pass through. This window is then covered by the sample which is held in place by a custom-made sample holder.

The backside of the sample holder consists of a 0.5 mm thick copper plate which is electrically sealed to the chamber using copper tape. A circular hole, 18 cm in diameter, is cut in the center of the copper plate to allow signals to pass. The samples are then made large enough to completely cover this hole. Plexiglas panes are used on either side of the sample to hold it in place and ensure uniform thickness across the hole, see Figure 2. The Plexiglas pane in front of the sample is 3.175 mm thick while the pane attached to the copper plate is 0.5 mm thick and ensures that the sample does not fall through hole cut in the plate.

The complex ε_i for the samples was measured using an Agilent 85070E dielectric probe which was accurately calibrated to a DI water sample. Details on the accuracy of such measurement techniques can

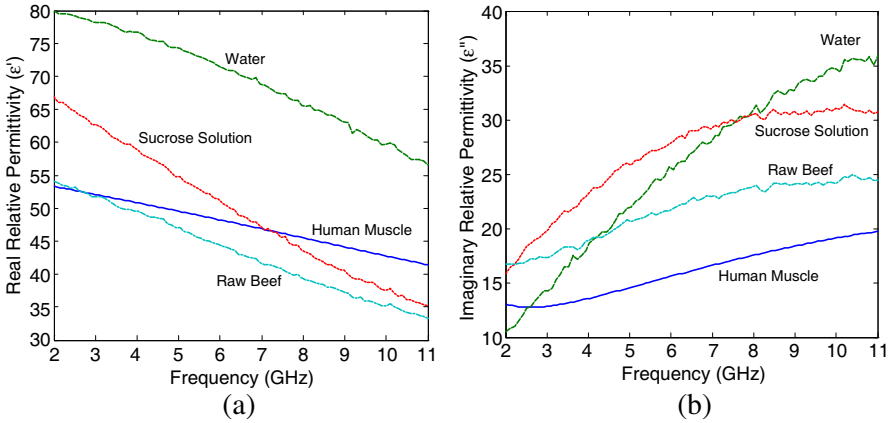

Figure 4. The relative (a) real and (b) imaginary permittivity of the water, sucrose and raw beef samples used in the measurements. The values were measured using an Agilent 85070E dielectric probe. Reported values for human muscle from [27] are also shown for comparison.

be found in [25]. The results are shown in Figure 4. The materials tested include water, raw beef and a sucrose solution. The sucrose solution ($C_{12}H_{22}O_{11}$, 1.0 mol/l) was used because it is known to be an accurate body phantom for human tissue across the UWB band [26].

3.2. Model Implementation

The model described in Section 2 was implemented using Matlab. For biological material such as that with which the human body is composed, $\mu_i = 1$. The complex ε_i for various human tissues at a wide range of frequencies can be found in the literature [27]. These values combined with (2), (8), (11) and (14)–(19) constitute a set of equations which allow for the calculation of attenuation and reflection due to the multilayer structure of the body. The source and load medium for the measurement setup is freespace, so those parameters are used within the model.

3.3. Measurement Results

In Figure 5 both modeled and measured attenuation, as defined in (19), are shown for water samples of two different thicknesses, 15.5 mm and 22.5 mm. The samples were placed in Ziploc bags which were then placed in the sample holder, tests showed that the bags had a negligible

affect on the results at these frequencies. A_{sl_air} was both calculated and measured ($|S_{21\,\mathrm{air}}|^2$) with only the bag and sample removed, thus the effect of the Plexiglas panes on the attenuation was taken into account. The results match well up to approximately 8–9 GHz at which point the loss becomes large and the noise floor of the measurement setup is reached. Up to this point the model predicts the measurement with errors of 4.8% and 1.4% for the 15.5 mm and 22.5 mm cases respectively. Here error is defined as

$$\mathrm{error} = 100 \left| \frac{\sum\limits_f A_{\mathrm{model}} - \sum\limits_f A_{\mathrm{measured}}}{\sum\limits_f A_{\mathrm{measured}}} \right| \tag{20}$$

where f indicates that the summation is made across the relevant frequency band normalized to the number of points included in the summation.

To verify the model using material which more closely resembles the tissue encountered in implant situations, raw beef samples were tested, Figure 5. In this case the measurements were above the noise floor of the measurement setup and thus the analytical model matches very closely with the measured results across the UWB band. Errors in this case were 1.6% and 0.6% for the 8.8 and 11 mm case respectfully.

A four layer sample was also tested to verify the model's ability to predict attenuation of inhomogeneous materials. The results shown in Figure 6 once again match quite accurately, until the noise floor is reached at ~ 6.5 GHz. The error computed from 2–6.5 GHz is $\sim 7\%$. The layer structure is depicted in the inset of Figure 6 and consists of

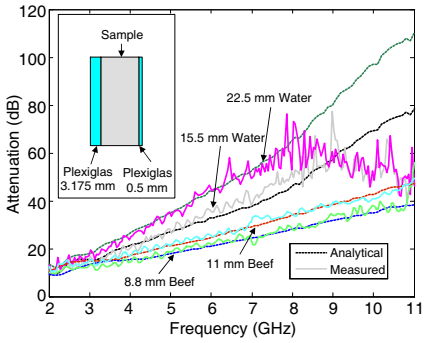

Figure 5. Analytical and measured results for water and beef samples of varying thickness.

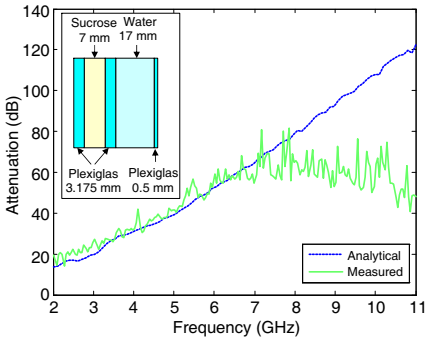

Figure 6. Analytical and measured results for a mulitilayer sample consisting of sucrose, Plexiglas and water.

3.175 mm of Plexiglas-7 mm of sucrose solution-3.175 mm of Plexiglas-17 mm of water-0.5 mm of Plexiglas.

4. ABDOMINAL IMPLANT CASE STUDY

The proposed analytical model was used to investigate the attenuation encountered by a UWB signal as it traverses the abdominal wall. This particular region of the body was selected because there are numerous applications where abdominal implants supporting a high bandwidth UWB data link would be beneficial. For instance if a high definition video link could be supported, wireless surgical cameras for laparoscopic surgery or ingestible cameras for gastrointestinal tract examination could provide real-time video to doctors and surgeons.

4.1. Layer Structure

Detailed cross-sectional images of the entire human body extracted via ultrasound or radiography are readily available [28, 29]. Figure 7 displays the layer model used for this investigation. It is based on the visible human project from NIH [30]. Transverse slice a_vm1610 was

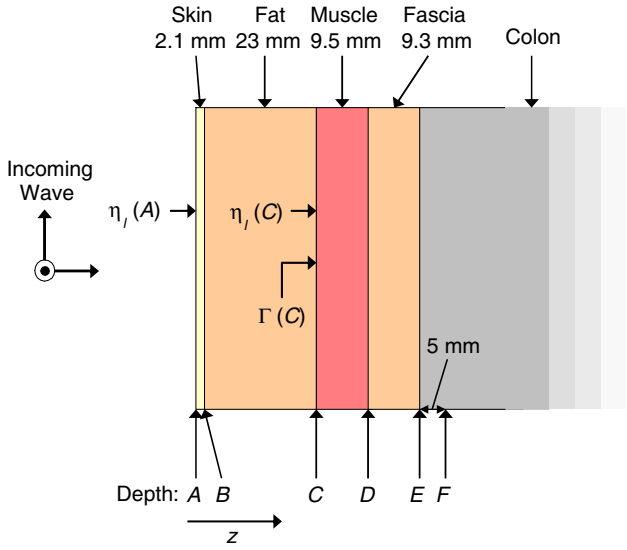

Figure 7. The layer structure of the anterior abdomen model based on the visible human project [30]. The colon is large and highly attenuative thus no further layers are modeled.

used to aid in the construction of this model [29]. The model represents the anterior abdominal wall, the layer structure is somewhat simplified for ease of implementation. The attenuation predictions from the analytical model of the layer structure in Figure 7 were compared to results from CST Microwave Studio, a commercial 3D finite integration technique (FIT) solver. In Microwave Studio, attenuation was found by simulating the loss of a plane wave of normal incidence as it traversed the multilayer structure. The dielectric properties of each layer were assumed to be homogeneous and equal to the values found in [27].

Referring to Figure 7, one sees that as signals traverse the abdomen wall toward the colon, they must pass through a layer of skin, fat, muscle and a layer loosely referred to as the fascia, a multilayer structure of fat and connective tissue. The model ends with the colon. Because it is large and provides high attenuation, no further layers were modeled. Since the analytical model describes the structure layer by layer, it is straightforward to calculate the attenuation at the interface between each tissue layer. Several interesting interfaces of interest and depths are labeled *A*–*F* on Figure 7.

4.2. Source and Load Impedance

In these tests, port 1 was assumed to be outside of the abdomen while port 2 was assumed to be inside. For the analytical model the source impedance, η_s, was set to that of freespace. Selecting the proper value for load impedance at depth z, $\eta_l(z)$, is somewhat less obvious. To first order the impedance can simply be set to the impedance of the following tissue. For example if calculating the attenuation down to depth $B(A(B))$ in Figure 7, $\eta_l(B)$ would be set to the impedance of fat; for $A(C)$, $\eta_l(C)$ would be set to the impedance of muscle and so forth. This is not entirely accurate because $A(z)$ depends on the standing wave ratio set up by the entire multilayer structure following depth z. For example $A(B)$ is affected by not only the next layer, muscle, but also the layer of fascia and the colon.

To calculate a more accurate value for $\eta_l(z)$, the overall reflection coefficient at depth z ($\Gamma(z)$) must be computed.

$$\Gamma(z) = \frac{\eta_l(z) - \eta_0(z)}{\eta_l(z) + \eta_0(z)} \tag{21}$$

Thus,

$$\eta_l(z) = \eta_0(z)\frac{1 + \Gamma(z)}{1 - \Gamma(z)}. \tag{22}$$

The reflection coefficient $\Gamma(z)$ can be found by first calculating the total transmission matrix model $[T'_z]$ for the layers following depth

z using (14) and (2). Next $[T'_z]$ can be converted to an S-parameter representation using the simple voltage formulations in [21]. Note that because impedance is concerned with the reflection of traveling waves and not power, the formulation found in the Appendix can not be applied. $\Gamma(z)$ is equal to S_{11} [21].

$$\Gamma(z) = \frac{\eta_{\text{last}} A'_z + B'_z - \eta_0(z)\eta_{\text{last}} C'_z - \eta_0(z) D'_z}{\eta_{\text{last}} A'_z + B'_z + \eta_0(z)\eta_{\text{last}} C'_z + \eta_0(z) D'_z} \tag{23}$$

Inserting (23) into (22) results in a simple expression for $\eta_l(z)$.

$$\eta_l(z) = \frac{\eta_{\text{last}} A'_z + B'_z}{\eta_{\text{last}} C'_z + D'_z} \tag{24}$$

In (21)–(23) $\eta_0(z)$ is the effective source impedance at depth z, its value is unimportant because it cancels out when (24) is computed. The impedance η_{last} represents the last or ending impedance in the layer structure.

The computation of $\eta_l(z)$ using (24) can be easily understood with the use of a simple example. Consider the layer structure of Figure 7, $\eta_l(C)$ represents the impedance looking into the muscle layer from the fat layer. When computing $A(C)$, the attenuation to depth C, it is necessary to calculate $\eta_l(C)$. The transmission matrix $[T'_C]$ can be computed using (2) and (14), $[T'_C] = [T'_{\text{muscle}}][T'_{\text{fascia}}]$. The impedance η_{last} should be set to the impedance of colon tissue. Plugging these values into (24) results in an accurate calculation of $\eta_l(C)$. This can then be used with (16) and (19) to calculate $A(C)$.

The selection of η_{last} and the number of layers to include in the calculation of $[T'_z]$ in the example above was quite obvious. For structures which have many layers following depth z, modeling all of them to calculate $\eta_l(z)$ can be cumbersome. Fortunately layers far down from z have little effect on $\eta_l(z)$ because the signal reaching them has been attenuated by the preceding layers. Thus one only needs to include a sufficient number of layers such that the signal has been attenuated enough to have little effect on $\eta_l(z)$. The question arises as to how much attenuation provides an accurate value. In Figure 8, the calculated $\eta_l(A)$ for the layer structure of Figure 7 versus the number of layers included in the $[T'_z]$ calculation is displayed. The calculation was done at 4 GHz. The number of layers included in the calculation is displayed on the top of the plot. For example at 3, the skin, fat and muscle layers are included in the $[T'_z]$ calculation and η_{last} is set to the impedance of fascia. The lower x-axis displays the attenuation caused by the layers up to that depth. As each layer is added starting with skin, the calculated impedance settles in to a single accurate value. From this one sees that ~ 20 dB of attenuation provides an accurate $\eta_l(z)$ calculation.

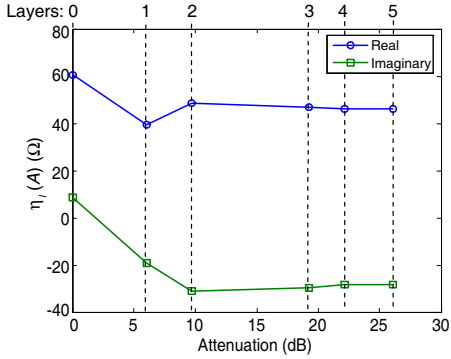

Figure 8. Calculated load impedance $\eta_l(A)$ of the structure shown in Figure 7 at 4 GHz versus the number of layers used in the calculation. The attenuation provided by the layers is shown on the x-axis.

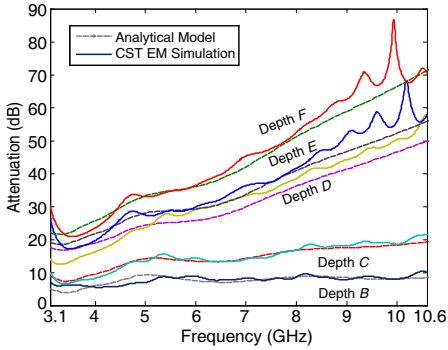

Figure 9. Analytical and simulated attenuation results for the abdomen model at the depths indicated in Figure 7.

4.3. Simulation Results

In Figure 9 the attenuation at depth B–F, as indicated in Figure 7, is shown. The results of the analytical model are compared to the results from Microwave Studio. The analytical model produces similar results while requiring far less computation time, approximately 5 seconds for the analytical model compared to 73 minutes for CST using 8 mesh lines per wavelength on a Pentium D 2.8 GHz machine with 3 GB of ram. The largest discrepancy between analytical and simulated results occurs at a resonance in the upper part of the band for the deeper implants. These appear to be artifacts of the simulation since they change in frequency and magnitude according to mesh size.

Unfortunately no reasonable meshing removes them completely. If these portions of the spectrum are ignored the error (20) between simulation and the proposed model is $< 5\%$ across all of the selected depths.

The results from this investigation give insight into the possibility of using UWB signals for abdominal implants. Signals addressing an implant just under the skin at B incur a relatively frequency-independent attenuation of ~ 8 dB. It is quite reasonable to expect that a loss of this magnitude could be accommodated within a designer's link budget. The next most interesting depth is E. At this point the implant is between the abdominal wall and the colon, within the abdominal cavity. This is the location at which abdominal orthoscopic surgery takes place and thus devices such as wireless cameras used during such procedures would sustain this level of attenuation. At this point the lower end of the spectrum is attenuated by ~ 20 dB, with the attenuation steadily increasing to ~ 56 dB at 10.6 GHz. This indicates that UWB signals which are located in the lower end of the spectrum will be able to traverse the abdominal wall with less attenuation and distortion. Depth F is also interesting, here the signal has penetrated 5 mm into the colon, about the thickness of the colon wall. Thus this roughly represents the location of a swallowable device. The attenuation here reaches all the way up to 70 dB at 10.6 GHz but at the lower frequencies is just over 20 dB. For this case it is likely that the designer would find it imperative that the signal avoids the higher end of the spectrum.

5. CONCLUSION

The attenuation of signals used to communicate with medical implants is modeled using transmission line theory. The model was verified experimentally for single and multilayer samples with errors of less than 5% and 7% respectfully. A realistic implant scenario was modeled with accuracy within 5% of a full 3D EM simulation but at significantly lower computation time. The proposed model provides a simple, fast and accurate way to predict the frequency dependent attenuation of RF signals used in medical implant communication. The results indicated that the higher frequency portion of the UWB band will be significantly attenuated by body tissue.

ACKNOWLEDGMENT

The authors would like to thank Qualcomm for their support with measurements and simulations.

APPENDIX A. DERIVATION OF EQUATIONS (16)–(18)

Figure A1 illustrates a media segment of impedance η and thickness d. The source and load media extend out infinitely from the segment and have impedances of η_s and η_l respectively. The following derivation allows for η_s and η_l to be complex, but requires that the real and imaginary parts of η_s and η_l be ≥ 0. This insures that $|S_{xy}| \leq 1$. The impedance of all biological material found in the human body satisfies this condition. E and H define the total electric and magnetic field at a given point. We will define that for both the forward (positive z-direction) and backward (negative z-direction) traveling waves the electric component points entirely in the positive x-direction. Meanwhile, for forward waves the magnetic component points entirely in the positive y-direction and for backward waves it points entirely in the negative y-direction. a and b define the incoming and outgoing power parameters at a given plane. These parameters are similar to "power waves" as defined in [22–24]. Here they are not referred to as waves because as pointed out in [23] and [24] these parameters differ fundamentally from traveling waves. Still they exhibit power transfer relationships which are useful to this work. The power parameters are defined by the following set of equations.

$$a_1 = \sqrt{\mathrm{Re}(\eta_s)}H_{1+} \tag{A1a}$$

$$b_1 = \sqrt{\mathrm{Re}(\eta_s)}H_{1-} \tag{A1b}$$

$$a_2 = \sqrt{\mathrm{Re}(\eta_l)}H_{2-} \tag{A1c}$$

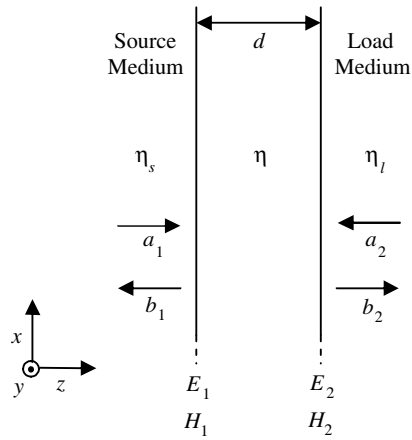

Figure A1. Transmission medium segment.

$$b_2 = \sqrt{\mathrm{Re}(\eta_l)}H_{2+} \tag{A1d}$$

$$E_{1+} = \eta_s^* H_{1+} \tag{A2a}$$
$$E_{1-} = \eta_s H_{1-} \tag{A2b}$$
$$E_{2+} = \eta_l H_{2+} \tag{A2c}$$
$$E_{2-} = \eta_l^* H_{2-} \tag{A2d}$$

In (25) and (26) (+) subscripts refer to components of waves that travel in the positive z-direction and (−) subscripts indicate wave components which travel in the negative z-direction. These equations satisfy the power relation: power into port i is equal to $\frac{1}{2}\left(|a_i|^2 - |b_i|^2\right)$. Furthermore when a port is complex conjugate matched there is no reflection, a attribute not true of traveling waves.

Using the definition of transmission parameters ($ABCD$) and scattering parameters (S) [18].

$$E_1 = AE_2 + BH_2 \tag{A3}$$
$$H_1 = CE_2 + DH_2 \tag{A4}$$
$$b_1 = S_{11}a_1 + S_{12}a_2 \tag{A5}$$
$$b_2 = S_{21}a_1 + S_{22}a_2 \tag{A6}$$

It must be noted here that using power parameters in (A5) and (A6) results in S-parameters which are only equivalent to standard S-parameters computed using traveling waves when η_s and η_l are real. On the other hand S-parameters computed using the parameters defined by (25) and (26) allow for the easy computation of the ratios of time-averaged power necessary for this work, even when η_s and η_l are complex. From (25), (A5) and (A6),

$$R_s = |S_{11}|^2 = \left|\frac{b_1}{a_1}|_{a_2=0}\right|^2 = \frac{\mathrm{Re}(\eta_s)\,|H_{1-}|^2}{\mathrm{Re}(\eta_s)\,|H_{1+}|^2} = \frac{\frac{1}{2}\mathrm{Re}\left(E_{1-}H_{1-}^*\right)}{\frac{1}{2}\mathrm{Re}\left(E_{1+}H_{1+}^*\right)} = \frac{P_{1-}}{P_{1+}}. \tag{A7}$$

Likewise,

$$R_l = |S_{22}|^2 = \left|\frac{b_2}{a_2}|_{a_1=0}\right|^2 = \frac{P_{2+}}{P_{2-}} \tag{A8}$$

$$A_{sl} = |S_{21}|^2 = \left|\frac{b_2}{a_1}|_{a_2=0}\right|^2 = \frac{P_{2+}}{P_{1+}} \tag{A9}$$

$$A_{ls} = |S_{12}|^2 = \left|\frac{b_1}{a_2}|_{a_1=0}\right|^2 = \frac{P_{1-}}{P_{2-}}. \tag{A10}$$

Also the electric and magnetic field can be written in terms of the

power parameters using (25) and (26).

$$E_1 = E_{1+} + E_{1-} = \frac{1}{\sqrt{\mathrm{Re}(\eta_s)}}\left(a_1\eta_s^* + b_1\eta_s\right) \tag{A11}$$

$$E_2 = E_{2+} + E_{2-} = \frac{1}{\sqrt{\mathrm{Re}(\eta_l)}}\left(b_2\eta_l + a_2\eta_l^*\right) \tag{A12}$$

$$H_1 = H_{1+} - H_{1-} = \frac{1}{\sqrt{\mathrm{Re}(\eta_s)}}(a_1 - b_1) \tag{A13}$$

$$H_2 = H_{2+} - H_{2-} = \frac{1}{\sqrt{\mathrm{Re}(\eta_l)}}(b_2 - a_2) \tag{A14}$$

Now inserting (A11)–(A14) into (A3) and (A4), E and H can be eliminated.

$$\frac{a_1\eta_s^* + b_1\eta_s}{\sqrt{\mathrm{Re}(\eta_s)}} = A\frac{b_2\eta_l + a_2\eta_l^*}{\sqrt{\mathrm{Re}(\eta_l)}} + B\frac{b_2 - a_2}{\sqrt{\mathrm{Re}(\eta_l)}} \tag{A15}$$

$$\frac{a_1 - b_1}{\sqrt{\mathrm{Re}(\eta_s)}} = C\frac{b_2\eta_l + a_2\eta_l^*}{\sqrt{\mathrm{Re}(\eta_l)}} + D\frac{b_2 - a_2}{\sqrt{\mathrm{Re}(\eta_l)}} \tag{A16}$$

A.1. Equation (16)

From (A6),

$$S_{21} = \frac{b_2}{a_1}|_{a_2=0}. \tag{A17}$$

Setting $a_2 = 0$ in (A15) and (A16),

$$\frac{a_1\eta_s^* + b_1\eta_s}{\sqrt{\mathrm{Re}(\eta_s)}} = A\frac{b_2\eta_l}{\sqrt{\mathrm{Re}(\eta_l)}} + B\frac{b_2}{\sqrt{\mathrm{Re}(\eta_l)}} \tag{A18}$$

$$\frac{a_1 - b_1}{\sqrt{\mathrm{Re}(\eta_s)}} = C\frac{b_2\eta_l}{\sqrt{\mathrm{Re}(\eta_l)}} + D\frac{b_2}{\sqrt{\mathrm{Re}(\eta_l)}}. \tag{A19}$$

Solving (A19) for b_1 and plugging it into (A18)

$$\begin{aligned} &a_1\eta_s^* + \eta_s\left(a_1 - C\frac{b_2\eta_l\sqrt{\mathrm{Re}(\eta_s)}}{\sqrt{\mathrm{Re}(\eta_l)}} - D\frac{b_2\sqrt{\mathrm{Re}(\eta_s)}}{\sqrt{\mathrm{Re}(\eta_l)}}\right) \\ = \; &A\frac{b_2\eta_l\sqrt{\mathrm{Re}(\eta_s)}}{\sqrt{\mathrm{Re}(\eta_l)}} + B\frac{b_2\sqrt{\mathrm{Re}(\eta_s)}}{\sqrt{\mathrm{Re}(\eta_l)}}. \end{aligned} \tag{A20}$$

Finally using (A17) and (A20) we can solve for S_{21}.

$$S_{21} = \frac{2\sqrt{\mathrm{Re}(\eta_s)}\sqrt{\mathrm{Re}(\eta_l)}}{\eta_l A + B + \eta_s\eta_l C + \eta_s D} \tag{A21}$$

Thus

$$A_{sl} = |S_{21}|^2 = \left| \frac{2\sqrt{\mathrm{Re}(\eta_s)}\sqrt{\mathrm{Re}(\eta_l)}}{\eta_l A + B + \eta_s \eta_l C + \eta_s D} \right|^2 . \tag{A22}$$

Note that by reciprocity $S_{12} = S_{21}$ and thus $A_{sl} = A_{ls}$ [24].

A.2. Equation (17)

From (A3),

$$S_{11} = \frac{b_1}{a_1}|_{a_2=0}. \tag{A23}$$

Solving (A19) for b_2 and plugging it into (A18)

$$\begin{aligned} \frac{a_1\eta_s^* + b_1\eta_s}{\sqrt{\mathrm{Re}(\eta_s)}} &= \frac{A\eta_l}{\sqrt{\mathrm{Re}(\eta_l)}} \left(\frac{\frac{a_1-b_1}{\sqrt{\mathrm{Re}(\eta_s)}}}{\frac{C\eta_l}{\sqrt{\mathrm{Re}(\eta_l)}} + \frac{D}{\sqrt{\mathrm{Re}(\eta_l)}}} \right) \\ &\quad + \frac{B}{\sqrt{\mathrm{Re}(\eta_l)}} \left(\frac{\frac{a_1-b_1}{\sqrt{\mathrm{Re}(\eta_s)}}}{\frac{C\eta_l}{\sqrt{\mathrm{Re}(\eta_l)}} + \frac{D}{\sqrt{\mathrm{Re}(\eta_l)}}} \right). \end{aligned} \tag{A24}$$

Now we can solve for S_{11} using (A23) and (A24).

$$S_{11} = \frac{\eta_l A + B - \eta_s^* \eta_l C - \eta_s^* D}{\eta_l A + B + \eta_s \eta_l C + \eta_s D} \tag{A25}$$

$$R_s = |S_{11}|^2 = \left| \frac{\eta_l A + B - \eta_s^* \eta_l C - \eta_s^* D}{\eta_l A + B + \eta_s \eta_l C + \eta_s D} \right|^2 \tag{A26}$$

A.3. Equation (18)

From (A6),

$$S_{22} = \frac{b_2}{a_2}|_{a_1=0}. \tag{A27}$$

Setting $a_1 = 0$ in (A15) and (A16),

$$\frac{b_1\eta_s}{\sqrt{\mathrm{Re}(\eta_s)}} = A\frac{b_2\eta_l + a_2\eta_l^*}{\sqrt{\mathrm{Re}(\eta_l)}} + B\frac{b_2 - a_2}{\sqrt{\mathrm{Re}(\eta_l)}} \tag{A28}$$

$$\frac{-b_1}{\sqrt{\mathrm{Re}(\eta_s)}} = C\frac{b_2\eta_l + a_2\eta_l^*}{\sqrt{\mathrm{Re}(\eta_l)}} + D\frac{b_2 - a_2}{\sqrt{\mathrm{Re}(\eta_l)}}. \tag{A29}$$

Solving (A28) for b_1 and plugging it into (A29)

$$-\frac{1}{\eta_s}\left(A\frac{b_2\eta_l + a_2\eta_l^*}{\sqrt{\mathrm{Re}(\eta_l)}} + B\frac{b_2 - a_2}{\sqrt{\mathrm{Re}(\eta_l)}} \right) = C\frac{b_2\eta_l + a_2\eta_l^*}{\sqrt{\mathrm{Re}(\eta_l)}} + D\frac{b_2 - a_2}{\sqrt{\mathrm{Re}(\eta_l)}}. \tag{A30}$$

Finally using (A27) and (A30) we can solve for S_{22}.

$$R_l = \frac{-\eta_l^* A + B - \eta_s \eta_l^* C + \eta_s D}{\eta_l A + B + \eta_s \eta_l C + \eta_s D} \tag{A31}$$

Thus

$$R_l = |S_{22}|^2 = \left| \frac{-\eta_l^* A + B - \eta_s \eta_l^* C + \eta_s D}{\eta_l A + B + \eta_s \eta_l C + \eta_s D} \right|^2 . \tag{A32}$$

Note that if $\eta_s = \eta_l = \eta_o$ where η_o is real (A21), (A25) and (A31) will reduce to the definitions found in many text books.

REFERENCES

1. Reichman, A., "Standardization of body area networks," *IEEE Int. Conf. COMCAS*, 1–4, Tel Aviv, Nov. 9–11, 2009.
2. Li, H.-B., K.-I. Takizawa, B. Zheri, and R. Kohno, "Body area network and its standardization at IEEE 802.15.MBAN," *16th IST Mobile and Wireless Commun. Summit.*, 1–5, Budapest, Jul. 1–5, 2007.
3. Wang, Q., K. Masami, and J. Wang, "Channel modeling and BER performance for wearable and implant UWB body area links on chest," *IEEE Int. Conf. ICUWB*, 316–320, Vancouver, BC, Sep. 9–11, 2009.
4. Dissanayake, T., M. R. Yuce, and C. Ho, "Design and evaluation of a compact antenna for implant-to-air UWB communication," *IEEE Antennas Wireless Propag. Lett.*, Vol. 8, 153–156, 2009.
5. Dissanayake, T., K. Esselle, and M. Yuce, "UWB antenna impedance matching in biomedical implants," *3rd European Conf. on Antennas and Propag.*, 3523–3526, Berlin, Mar. 23–27, 2009.
6. Klemm, M. and G. Troester, "EM energy absorption in the human body tissues due to UWB antennas," *Progress In Electromagnetics Research*, Vol. 62, 261–280, 2006.
7. Gemio, J., J. Parron, and J. Soler, "Human body effects on implantable antennas for ISM bands applications: Models comparison and propagation losses study," *Progress In Electromagnetics Research*, Vol. 110, 437–452, 2010.
8. Zasowski, T., G. Meyer, F. Althaus, and A. Wittneben, "UWB signal propagation at the human head," *IEEE Trans. Microw. Theory Tech.*, Vol. 54, No. 4, 1836–1845, Jun. 2006.
9. Chen, Y., et al. "Cooperative communications in ultra-wideband wireless body area networks: Channel modeling and system diversity analysis," *IEEE J. Sel. Areas Commun.*, Vol. 27, No. 1, 5–16, Jan. 2009.

10. Hao, Y., A. Alomainy, Y. Zhao, and C. Parini,, "UWB body-centric network: Radio channel characteristics and deterministic propagation modelling," *The Institution of Eng. and Technology Seminar on Ultra Wideband Sys., Technologies and Applicat.*, 160–164, London, Apr. 20, 2006.
11. O'Halloran, M., M. Glavin, and E. Jones, "Effects of fibroglandular tissue distribution on data-independent beamforming algorithms," *Progress In Electromagnetics Research*, Vol. 97, 141–158, 2009.
12. Zhu, G. K. and M. Popovic, "Comparison of radar and thermoacoustic technique in microwave breast imaging," *Progress In Electromagnetics Research B*, Vol. 35, 1–14, 2011.
13. Wang, J. and D. Su, "Design of an ultra wideband system for in-body wireless communications," *The 4th Asia-Pacific Conf. on Environmental Electromagnetics*, 565–568, Dalian, Aug. 1–4, 2006.
14. Khaleghi, A. and I. Balasingham, "On the ultra wideband propagation channel characterizations of the biomedical implants," *IEEE 69th Veh. Technol. Conf.*, 1–4, Barcelona, Apr. 26–29, 2009.
15. Thiel, F. and F. Seifert, "Noninvasive probing of the human body with electromagnetic pulses: Modeling of the signal path," *J. Appl. Phys.*, Vol. 105, No. 4, 044904–044904, Feb. 2009.
16. Varotto, G. and E. M. Staderini, "A 2D simple attenuation model for EM waves in human tissues: Comparison with a FDTD 3D simulator for UWB medical radar," *IEEE Int. Conf. on Ultra-Wideband*, Vol. 3, 1–4, Leibniz, Germany, Sep. 10–12, 2008.
17. Collin, R. E., *Foundations for Microwave Engineering*, 179–181, McGraw-Hill, New York, 1966.
18. Ramo, S., J. R. Whinnery, and T. van Duzer, *Fields and Waves in Communication Electronics*, 2nd edition, 285, John Wiley, New York, 1984.
19. Pozar, D. M., *Microwave Engineering*, 3rd edition, 187, Wiley, Hoboken, NJ, 2005.
20. Beatty, R. W. and D. M. Kerns, "Relationships between different kinds of network parameters, not assuming reciprocity or equality of the waveguide or transmission line characteristic impedances," *Proc. IEEE*, Vol. 52, 84, Jan. 1964.
21. Kerns, D. M. and R. W. Beatty, *Basic Theory of Waveguide Junctions and Introductory Microwave Network Analysis*, 136–139, Pergamon, Elmsford, NJ, 1967.

22. Frickey, D. A., "Conversions between S, Z, Y, h, $ABCD$, and T parameters which are valid for complex source and load impedances," *IEEE Trans. Microw. Theory Tech.*, Vol. 42, No. 2, 205–211, Feb. 1994.
23. Marks, R. B. and D. F. Williams, "Comments on conversions between S, Z, Y, h, $ABCD$, and T parameters which are valid for complex source and load impedances," *IEEE Trans. Microw. Theory Tech.*, Vol. 43, No. 4, 914–915, Apr. 1995.
24. Marks, R. B. and D. F. Williams, "A general waveguide circuit theory," *J. Res. Natl. Inst. Stand. Technol.*, Vol. 97, 533–561, Sep.–Oct. 1992.
25. Wang, Z., W. Che, and L. Zhou, "Uncertainty analysis of the rational function model used in the complex permittivity measurement of biological tissues using PMCT probes within a wide microwave frequency band," *Progress In Electromagnetics Research*, Vol. 90, 137–150, 2009.
26. Yamamoto, H., J. Zhou, and T. Kobayashi, "Ultra wideband electromagnetic phantoms for antennas and propagation studies," *IEICE Trans. Fundamentals*, Vol. E91-A, No. 11, Nov. 2008.
27. Andreuccetti, D., R. Fossi, and C. Petrucci, "Dielectric properties of body tissues," IFAC-CNR, Florence, Italy, 1997–2007. Available: http://niremf.ifac.cnr.it/tissprop/#over.
28. Kieffer, S. A. and E. R. Heitzman, *An Atlas of Cross-sectional Anatomy*, Harper and Row, Hagerstown, ML, 1979.
29. Spitzer, V. M. and D. G. Whitlock, *Atlas of the Visible Human Male*, Jones and Bartlett, Sudbury, MA, 1998.
30. Ackerman, M. J., "The visible human project," *Proc. IEEE*, Vol. 86, No. 3, 504–511, Mar. 1998.